doi:10.1016/j.jmb.2005.02.008 J. Mol. Biol. (2005) 347, 965–978

JMB

Available online at www.sciencedirect.com

SCIENCE DIRECT®

ELSEVIER

Evidence for Structural Plasticity of Heavy Chain Complementarity-determining Region 3 in Antibody–ssDNA Recognition

Jonathan P. Schuermann[1], Season P. Prewitt[1], Christopher Davies[2] Susan L. Deutscher[3] and John J. Tanner[1,3]*

[1]*Department of Chemistry University of Missouri-Columbia, Columbia MO 65211, USA*

[2]*Department of Biochemistry and Molecular Biology, Medical University of South Carolina Charleston, SC 29425, USA*

[3]*Department of Biochemistry University of Missouri-Columbia, Columbia MO 65211, USA*

**Corresponding author*

Anti-DNA antibodies play important roles in the pathogenesis of autoimmune diseases. They also represent a unique and relatively unexplored class of DNA-binding protein. Here, we present a study of conformational changes induced by DNA binding to an anti-ssDNA Fab known as DNA-1. Three crystal structures are reported: a complex of DNA-1 bound to dT_3, and two structures of the ligand-free Fab. One of the ligand-free structures was determined from crystals exhibiting perfect hemihedral twinning, and the details of structure determination are provided. Unexpectedly, five residues (H97–H100A) in the apex of heavy chain complementarity-determining region 3 (HCDR3) are disordered in both ligand-free structures. Ligand binding also caused a 2–4 Å shift of the backbone of Tyr L92 and ordering of the L92 side-chain. In contrast, these residues are highly ordered in the Fab/dT_3 complex, where Tyr H100 and Tyr H100A form intimate stacking interactions with DNA bases, and L92 forms the 5′ end of the binding site. The structures suggest that HCDR3 is very flexible and adopts multiple conformations in the ligand-free state. These results are discussed in terms of induced fit and pre-existing equilibrium theories of ligand binding. Our results allow new interpretations of existing thermodynamic and mutagenesis data in terms of conformational entropy and the volume of conformational space accessible to HCDR3 in the ligand-free state. In the context of autoimmune disease, plasticity of the ligand-free antibody could provide a mechanism by which anti-DNA antibodies bind diverse host ligands, and thereby contribute to pathogenicity.

Keywords: anti-DNA antibodies; X-ray crystallography; systemic lupus erythematosus; hemihedral twinning; DNA-binding proteins

Introduction

Anti-DNA antibodies (Abs) are part of the aberrant immune response associated with systemic lupus erythematosus (SLE) and other autoimmune diseases.[1–3] Anti-DNA Abs directly contribute to the kidney inflammation associated with SLE through several possible mechanisms, including, binding to DNA immobilized to the glomerular basement membrane (GBM), nucleosome-mediated anti-DNA Ab deposition in the GBM, and cross-reaction of anti-DNA Abs with non-DNA glomerular components.[2,4–11] Because of their important role in SLE pathology, the presence of abnormal levels of anti-DNA Abs in sera is one of the indicators used in diagnosing SLE.

Compounds that bind to pathogenic anti-DNA Abs and prevent their deposition in tissues could be potentially useful therapeutic agents for treatment of SLE.[3,12–14] Anti-DNA Abs represent a challenging ligand design target, however, due to their inherent cross-reactivity. Several studies have reported the binding of non-DNA ligands to

Abbreviations used: Ab, antibody; Fab, antigen binding fragment; CDR, complementarity-determining region; SLE, systemic lupus erythematosus; PDB, Protein Data Bank; V, variable; C, conserved; H, heavy; L, light; RMSD, root-mean-square difference; CC, correlation coefficient; ss, single-stranded.

E-mail address of the corresponding author: tannerjj@missouri.edu

anti-DNA Abs, including anionic dyes,[15] benzodiazepines,[8] pneumococcal polysaccharide,[16] phosphorylcholine,[16,17] the protein α-actinin,[18] acidic pentapeptides,[19] the NR2 glutamate receptor,[20] Cys-constrained 16-mer peptides,[21] histones,[21] and nucleosomes.[2,21] Thus, it is crucially important to elucidate the mechanisms by which anti-DNA Abs recognize diverse ligands in order to understand the roles that anti-DNA Abs play in autoimmune disease pathology, and for inhibitor design.

Our focus in the anti-DNA Ab field has been a recombinant anti-ssDNA Fab, known as DNA-1, that was isolated from a combinatorial bacteriophage display library of IgG fragments derived from the immunoglobulin repertoire of an autoimmune SLE-like MRL/lpr mouse.[22] The genes encoding DNA-1 light (L) and heavy (H) chains are closely related to gene families $V_\kappa 12$[23,24] and V_H J558,[25] respectively, based on nucleotide sequence similarity analysis using the IMGT database.[26] Along with 11F8[27–31] and BV04-01,[32] DNA-1 is among the best characterized anti-DNA antibodies in terms of structure, specificity, and affinity. Like 11F8 and BV04-01, DNA-1 displays a strong preference for binding thymine-rich single-stranded (ss) DNA ligands, with no detectable binding to double-stranded (ds) DNA.[33,34]

We previously reported the crystal structure of DNA-1 bound to dT_5.[35] This structure revealed the details of Ab–ssDNA interaction, and allowed us to identify conserved structural features of ssDNA recognition. However, our understanding of ligand recognition was incomplete because structures of the ligand-free Fab were not available. In particular, it was not known whether ligand binding induced conformational changes in the Fab. This missing information is critical, because conformational change could potentially help explain the cross-reactive nature of anti-DNA Abs.

To address this issue, we report three new crystal structures of Fab DNA-1: a DNA-1/dT_3 complex and two ligand-free structures. The structures reveal dramatic conformational changes caused by ligand binding, including, conformational ordering of heavy (H) chain complementarity-determining region 3 (HCDR3), a 4 Å movement of the backbone of light (L) chain CDR3, and stabilization of the side-chain of Tyr L92. These results point to CDR loop plasticity as a possible factor underlying anti-DNA Ab cross-reactivity, and therefore, pathogenicity.

Results

Three structures of Fab DNA-1 are presented:

Table 1. Data collection and refinement statistics

	DNA-1/dT_3	DNA-1/dT_3	$P6_5$	$P321$
PDB accession code	1XF2	N/A	1XF3	1XF4
Ligand	dT_3	dT_3	None	None
Wavelength (Å)	1.000	1.542	1.072	1.072
Space group	$P6_522$	$P6_522$	$P6_5$	$P321$
Unit cell dimensions (Å)	$a=170.7$	$a=170.7$	$a=201.8$	$a=179.2$
	$c=144.7$	$c=144.8$	$c=44.8$	$c=91.9$
No. of Fabs per asymmetric unit	2	2	2	2
Diffraction resolution (Å)	99–2.3	99–2.8	50–2.3	50–2.5
Outer shell (Å)	2.38–2.30	2.90–2.80	2.38–2.30	2.59–2.50
No. of observations	569,717	1,329,665	233,009	296,346
No. of unique reflections	55,433	31,222	46,702	51,454
Redundancy	10.3	42.6	5.0	5.8
Completeness (%)	99.9 (99.7)	99.9 (100.0)	99.8 (99.9)	87.0 (81.4)
Mean I/σ_I	30.8 (4.7)	69.5 (18.1)	16.3 (3.6)	13.3 (2.9)
R_{merge}	0.070 (0.446)	0.091 (0.359)	0.085 (0.455)	0.090 (0.511)
No. of protein atoms	6449		6357	6320
No. of water molecules	220		66	35
R_{cryst}	0.201 (0.216)		0.209 (0.300)	0.183 (0.216)
R_{free}[a]	0.242 (0.246)		0.241 (0.314)	0.224 (0.261)
Coordinate error (Å)	0.13		0.17	0.18
RMSD bond lengths (Å)[b]	0.013		0.013	0.014
RMSD bond angles (deg.)[b]	1.4		1.2	1.5
Ramachandran plot[c]				
Favored (%)	89.6		89.7	87.1
Allowed (%)	9.5		9.1	11.9
Generous (%)	0.5		0.7	0.4
Disallowed (%)	0.4		0.6	0.6
Average B-factors (Å^2)				
Protein	18.4		19.9	14.5
Solvent	46.5		43.5	18.6
Ligand	31.7		N/A	N/A

Values for the outer resolution shell of data are given in parentheses.
[a] 5% R_{free} test sets were used in refinement of the dT_3 and $P6_5$ structures. A 10% test set was used in refinement of the $P321$ structure.
[b] Compared to the Engh and Huber force field.[82]
[c] The Ramachandran plot was generated with PROCHECK.[83]

a 2.3 Å resolution DNA-1/dT_3 complex, a 2.3 Å resolution ligand-free structure with space group $P6_5$, and a second ligand-free structure determined at 2.5 Å resolution in space group *P*321 (Table 1). All three structures have two Fabs per asymmetric unit. The two Fabs in each asymmetric unit will be referred to as Fab 1 and Fab 2, with the light/heavy chains of Fab 1 and Fab 2 denoted L/H and A/B, respectively. The residue numbering scheme and complementarity-determining region (CDR) definitions used here follow the standard Kabat conventions.[36,37]

Structure determinations of the dT_3 complex and the $P6_5$ ligand-free structure were straightforward; however, perfect hemihedral twinning complicated solution of the *P*321 crystal form. Although several protein structures have been solved using twinned crystals, the use of twinned data is still somewhat uncommon.[38–42] Therefore, some of the details of structure determination are presented in Materials and Methods. Despite the complications due to twinning, the *P*321 structure could be elucidated through exhaustive molecular replacement trials in several space groups, followed by detwinning of the diffraction data using the correct molecular replacement solution. The resulting electron density maps were quite clear and readily interpretable (Figure 1), and allowed unambiguous modeling of the entire structure except residues 127–133 of the heavy chain, which are disordered in many Fab structures, and HCDR3 (discussed below).

dT_3 binding site

Electron density maps clearly indicated the presence of a DNA ligand bound to Fab 1 of the DNA-1/dT_3 structure (Figure 2). The locations of phosphate moieties were confirmed by anomalous difference Fourier maps calculated using highly redundant data collected using an in-house CuK_α system. This map clearly indicated the locations of two of the three expected phosphate groups (Figure 2). The electron density maps allowed unambiguous modeling of all but the 3′ nucleoside of dT_3, which is presumably disordered.

As observed in the DNA-1/dT_5 structure,[35] a second electron density feature suggested the presence of a single thymine nucleoside bound to Fab 2. However, the density was rather weak, and attempts to model DNA into this site resulted in *B*-values greater than 80 $Å^2$. Therefore this site was left unoccupied. Despite weak ligand binding, HCDR3 is well ordered in Fab 2, which could be due, in part, to crystal packing interactions. For reference, the average *B*-values for HCDR3 of Fabs 1 and 2 are 21 $Å^2$ and 26 $Å^2$, respectively. The HCDR3 conformations of the two Fabs are rather different, as evidenced by a backbone root-mean-square difference (RMSD) of 2.1 Å. These conformational differences were likewise observed in the DNA-1/dT_5 structure, and they have been discussed in detail previously.[35]

The dT_3 ligand binds in the previously identified dT_5 binding site,[35] with the T1 and T2 nucleotides of

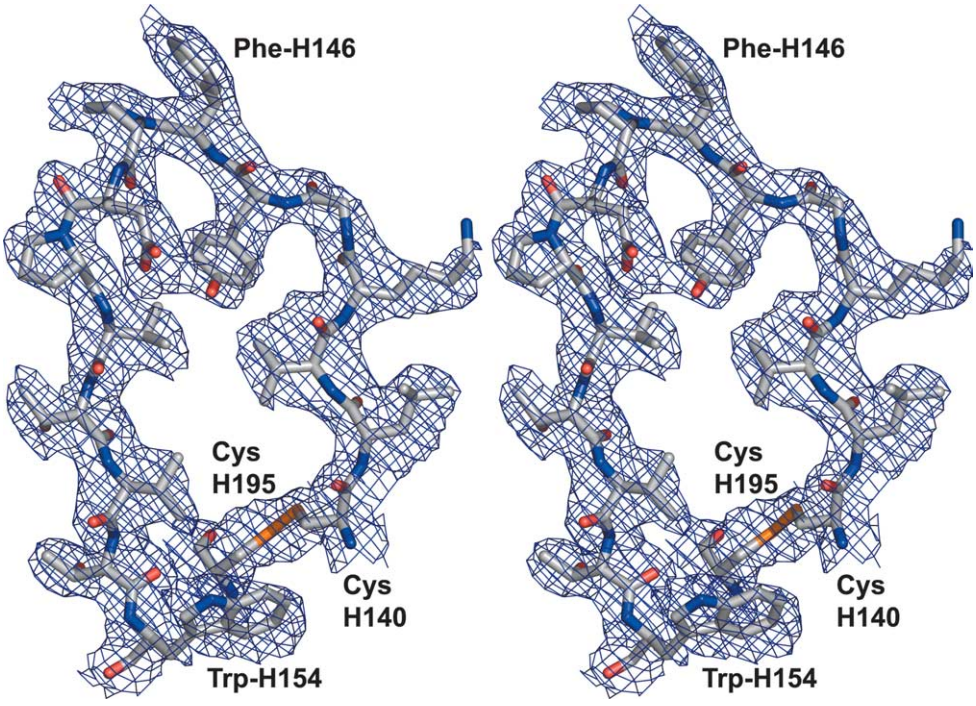

Figure 1. Stereo-view of residues H140–H154, and H195 of the *P*321 structure, covered by a σ_A-weighted $mF_o - DF_c$ electron density map (2.5σ). The pictured residues, as well as surrounding residues within 3.9 Å, were omitted prior to simulated annealing refinement and map calculation. This and other Figures were prepared with Pymol.

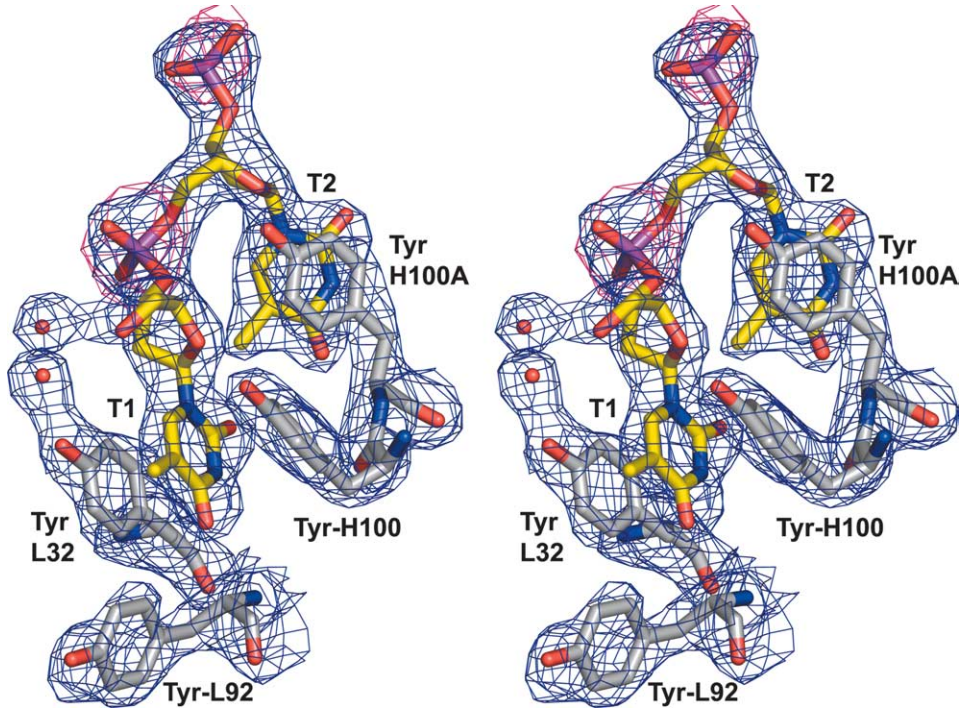

Figure 2. Stereo-view of the dT_3 binding site. The protein is white; DNA is colored yellow. A σ_A-weighted $mF_o - DF_c$ electron density map is shown in blue (3σ). The dT_3 ligand and surrounding residues within 3.9 Å were omitted prior to simulated annealing refinement and map calculation. Shown in pink is an anomalous difference Fourier map (2.5σ) calculated from data collected using CuK_α radiation.

dT_3 occupying the T2 and T3 binding sites, respectively, of the DNA-1/dT_5 structure. As in the DNA-1/dT_5 structure, the ssDNA adopts an extended conformation, with its bases buried in the protein and its phosphoribose backbone facing away from the protein surface (Figure 3). The binding site is formed by all six CDRs except HCDR1 and HCDR2 (Figure 3). The predominant theme of the binding site is the sandwiching of thymine bases between tyrosine side-chains (Figures 3 and 4). Specifically, the base of T1 inserts between Tyr L32 and Tyr H100, while T2 is sandwiched between Tyr L49 and Tyr H100A.

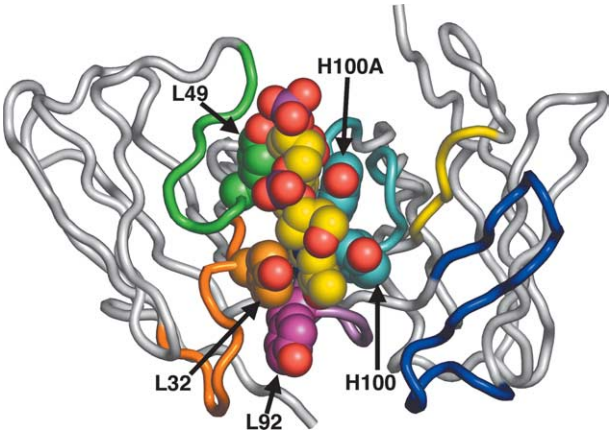

Figure 3. Ribbon drawing of Fab 1 of the DNA-1/dT_3 complex highlighting CDR usage and stacking of Tyr side-chains against DNA bases. DNA and Tyr side-chains are shown in a space-filling representation. DNA appears in yellow. The CDRs are color coded as follows: LCDR1, orange; LCDR2, green; LCDR3, purple; HCDR1, yellow; HCDR2, blue; and HCDR3, cyan.

In addition to these non-polar interactions, the DNA bases make four hydrogen bonds to the protein (Figure 4). The O2 carbonyl of T1 hydrogen bonds to the side-chain of His L91, while the O4 carbonyl hydrogen bonds to the backbone of Gly L93. The N–H of the T1 base hydrogen bonds to the backbone carbonyl of L91. The base of T2 forms a single hydrogen bond to the protein, with the O4 carbonyl hydrogen bonding to the backbone amine of Ala H100B. The lower *B*-values of T1 (27 $Å^2$) compared to T2 (33 $Å^2$) are probably due to the larger number of hydrogen bonds formed by T1.

The binding site features only one interaction with the DNA backbone. The side-chain of Asn L50 hydrogen bonds to the phosphate that connects T1 and T2 (Figure 4). The lack of interactions with the DNA backbone is consistent with the fact that the backbone faces away from the protein surface.

Finally, there is also a hydrogen bond between the hydroxyl of Tyr L32 and the 5′–OH of dT_3, which is mediated by two tightly bound water molecules (Figure 4). Electron density for these water molecules was quite strong and the *B*-values were reasonably low (37 $Å^2$, 41 $Å^2$, Figure 2). We note, however, that these water molecules are also stabilized by crystal contacts, and thus their contribution to binding is unclear.

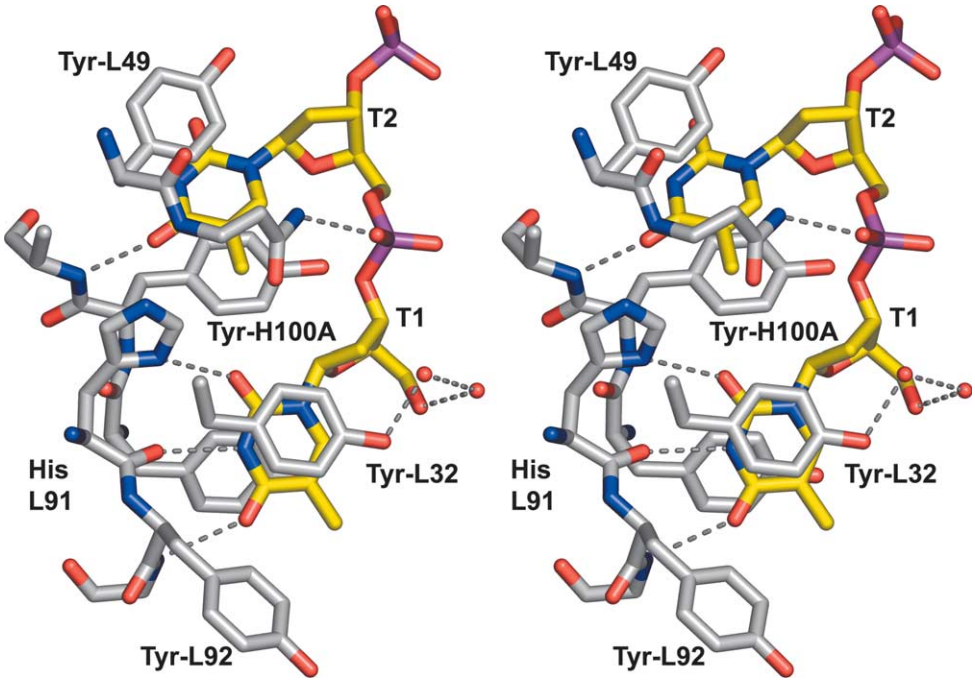

Figure 4. Stereo-view of the dT_3 binding site highlighting protein–DNA interactions. The protein appears in white, and the DNA appears in yellow. The broken lines represent hydrogen bonds.

Ligand-free structures

Two crystal forms of the ligand-free Fab were obtained. Since each crystal form contains two Fabs per asymmetric unit, the two structures provide four independent views of the ligand-free binding site. The ligand-free structures were compared to Fab 1 of DNA-1/dT_3 to identify structural changes caused by ligand binding. Two types of structural changes were analyzed: domain movement and local motion of CDRs.

The elbow angles for the DNA-1/dT_3 and *P*321 structures are very similar, and in the range 150–153°. In contrast, the elbow angles of the two Fabs in the $P6_5$ structure are 175–177°. Thus, there is no correlation between ligand binding and elbow angle. The differences in elbow angle are most likely due to the different crystal packing interactions. The three structures display small quaternary structural differences within the V_H/V_L superdomains. Using Fab 1 of DNA-1/dT_3 as the reference structure, the ligand-free structures display 5–6° relative rotations of the V_H and V_L domains. These changes are not necessarily due to ligand binding, because domain rotations of 4–5° are also observed when comparing the two ligand-free structures to each other. Thus, we were unable to find any domain movements associated with ligand binding.

The overall polypeptide chain conformations within the immunoglobulin domains of the three structures are very similar. The RMSDs between CA atoms of the ligand-free Fabs and Fab 1 of DNA-1/dT_3 are 0.4–0.5 Å for V_L and 0.4 Å for V_H. The RMSDs within C_L and C_H1 are 0.3–0.5 Å. Comparing the two ligand-free structures to each other, one finds RMSDs of 0.4–0.5 Å within the individual domains. Thus, overall backbone RMSDs are insensitive to ligand binding. Likewise, the RMSDs for all CDRs except LCDR3 and HCDR3 are quite small, indicating that these loops do not move significantly in response to ligand binding. Specifically, the RMSDs between CDRs of the ligand-free structures and Fab 1 of DNA-1/dT_3 are below 0.3 Å for LCDR1, LCDR2, HCDR1, and HCDR2.

In contrast, the RMSDs for LCDR3 are 0.6–0.9 Å. These higher values reflect a 2–4 Å movement of Tyr L92 (Figure 5). In the absence of ligand, L92 blocks the T1 binding site, and thus its movement is necessary for the ligand to enter the binding site. Electron density for the main chain of L92 was strong in all four unliganded Fab structures, but the side-chain density was very weak, which suggested that this side-chain is disordered in the absence of bound ligand. In the DNA-dT_3 structure; however, density for both the main chain and side-chain of L92 was strong and unambiguous (Figure 2). Note that L92 plays an important role in ligand recognition by forming the 5′ end of the binding site, where it contacts T1 (Figures 3–5).

The most dramatic conformational change caused by ligand binding occurred in HCDR3. Electron density representing the upper half of HCDR3 ($^{97}Y^{98}R^{99}P^{100}Y^{100A}Y$) was very weak in all four ligand-free Fabs. Consider, for example, the simulated annealing, σ_A-weighted $F_o - F_c$ map for HCDR3 of Fab 2 of the $P6_5$ structure (Figure 6(a)). Electron density representing residues B98–B100A was completely lacking at the 3σ contour level,

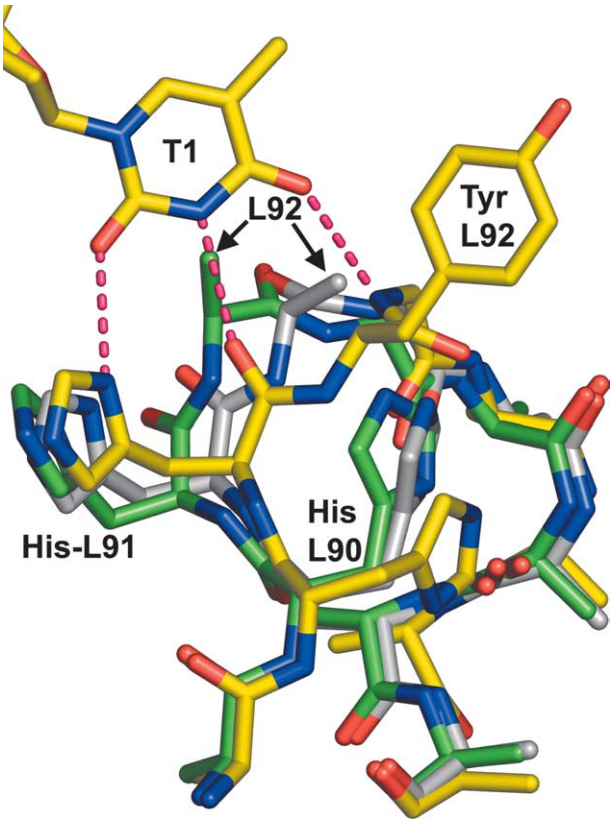

Figure 5. Superposition of LCDR3 from the two ligand-free Fabs onto LCDR3 of DNA-1/dT_3. The $P6_5$ and $P321$ structures are shown in green and white, respectively. The DNA-1/dT_3 complex is colored yellow. For each structure, the backbone of residues L89–L97 and the side-chains of His L90, His L91, and Tyr L92 are shown. Note that the side-chain of L92 is disordered in the two unliganded structures, and therefore it does not appear in the Figure.

and thus these residues were presumed to be disordered. Also, density for the side-chain of Tyr B97 was absent, although the main chain could be modeled (Figure 6(a)). In contrast, the maps clearly indicated the conformation of the lower half of the loop (residues B93–96 and B100B–B102). In particular, note that the density for the salt link at the base of the loop involving Arg B94 and Asp B101 was quite strong (Figure 6(a)). A similar situation was observed for HCDR3 of Fab 1 of the $P6_5$ structure. The density was weak for the apical residues of the loop, which prevented us from including Arg H98, Pro H99, Tyr H100, as well as the side-chains of Tyr H97 and Tyr H100A in the final model.

The $P321$ structure also suggested that HCDR3 is disordered in the absence of bound ligand. Electron density representing H98–H100A of Fab 1 was completely lacking (Figure 6(b)), and thus these residues were omitted from the final model. As with the $P6_5$ structure, the side-chain of Tyr H97 appears to be disordered. A similar situation was encountered in Fab 2 of the $P321$ structure. Density for residues B97–B100 was very weak, and these residues could not be modeled accurately.

We thus concluded that the apical residues of HCDR3 ($^{97}Y^{98}R^{99}P^{100}Y^{100A}Y$), as well as the side-chain of Tyr L92, are disordered in the absence of bound ligand. This is a very significant result because Tyr H100, Tyr H100A, and Tyr L92 are highly ordered in the dT_3 complex (Figure 2), and they form important non-polar interactions with thymine rings of dT_3 (Figures 3 and 4).

While the apex of HCDR3 is disordered in the ligand-free structures, the base of HCDR3 is well ordered, as evidenced by the strong electron density observed for heavy chain residues 93–96 and 100B–102 for all four Fabs of the two ligand-free crystal forms (Figure 6). The conformation of residues 93–96 and 100B–102 in the free state is very similar to that in the dT_3-bound state (RMSD = 0.5–0.7 for CA atoms; RMSD = 0.7–1.0 Å for all atoms). Thus, the base of HCDR3 is rather rigid, compared to the apex.

Discussion

DNA-1/dT_3 structure

DNA-1 binds oligo(dT) ligands of various lengths, from dT_3 to dT_{15}. The DNA-1/dT_3 structure shows that the dT_3 binding site is a subset of the dT_5 binding site, with T1 and T2 of dT_3 occupying the T2 and T3 binding sites of the DNA-1/dT_5 structure. There are no significant conformational differences between the dT_3 and dT_5 complexes within the binding site. Since dT_3 is the smallest oligo(dT) ligand believed to be recognized by DNA-1, the dT_3 binding site described here represents the essential recognition locus of DNA-1. This recognition locus consists of a narrow groove formed by the tyrosine side-chains of L32, H49, H100, and H100A, with hydrogen bond interactions provided by the side-chains of His L91 and Asn L50, and the main chain of HCDR3 and LCDR3. Presumably, this binding site is formed in all DNA-1/oligo(dT) complexes.

Glick's group has done seminal work in elucidating the principles of Ab–ssDNA recognition using Fab 11F8, which was obtained from a panel of anti-DNA monoclonal antibodies from an autoimmune MRL MpJ-lpr/lpr mouse. Using an *in vitro* evolution approach, they found that 11F8 binds with high specificity and nanomolar affinity to a stem–loop DNA ligand.[28] Mutagenesis of the stem–loop and chemical protection studies have been used to identify bases critical for binding,[29] and protection footprinting and site-directed mutagenesis of the Fab have been used to infer Ab–DNA contacts.[30] Their work showed that 11F8 contacts two consecutive T nucleotides of the loop; however, there are no crystal structures of 11F8 in either the ligand-free form or bound to DNA. Since the DNA-1/dT_3 structure shows the Fab interacting with two

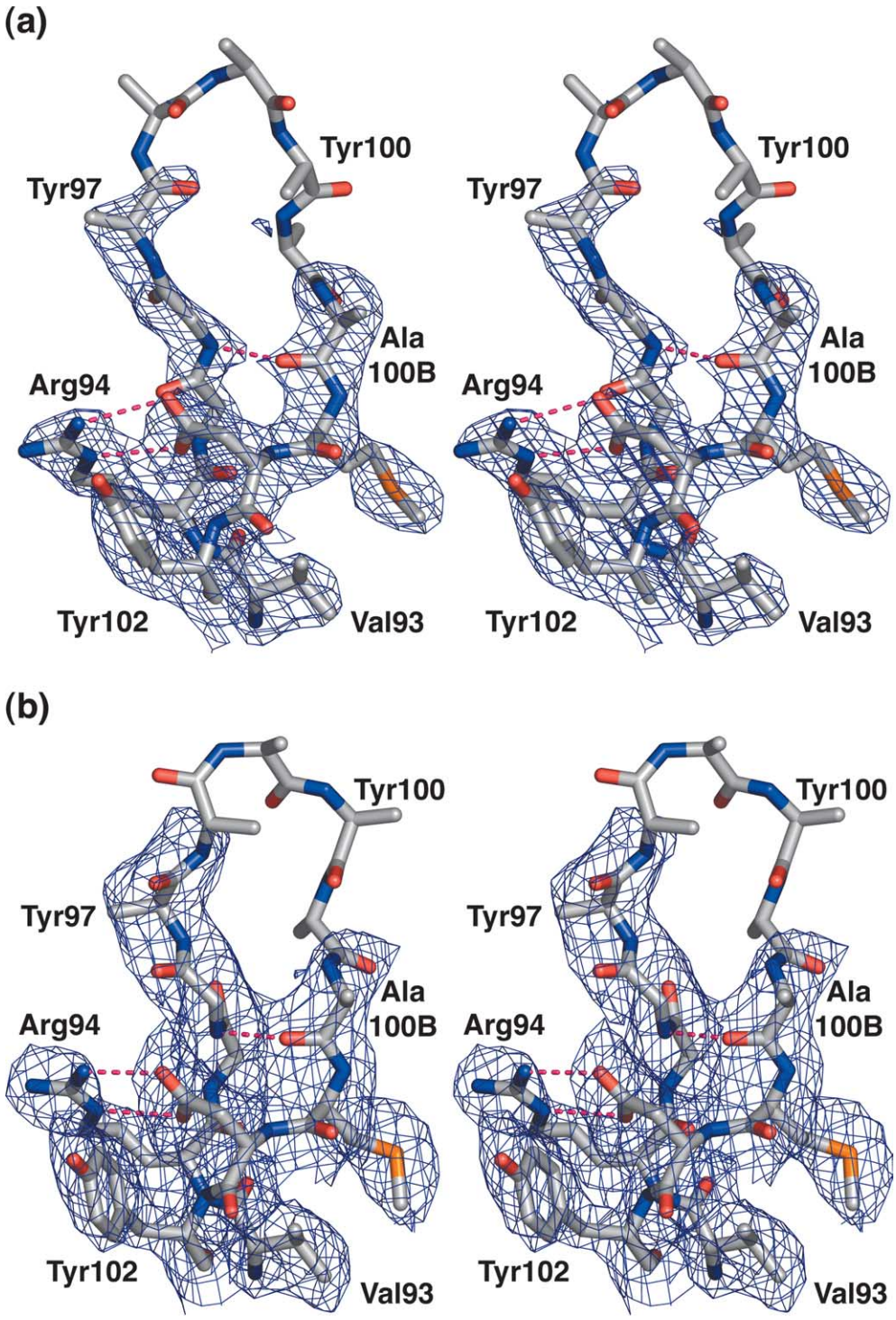

Figure 6. Stereo-views of heavy chain residues 93–102 from the two ligand-free structures, which includes HCDR3. For reference, the sequence of heavy chain residues 93–102 is ^{93}VRGGYRP^{100}Y^{100A}Y^{100B}A^{100C}MD^{102}Y. (a) HCDR3 from Fab 2 of the $P6_5$ structure. (b) HCDR3 from Fab 1 of the $P321$ structure. The electron density maps for both panels are simulated annealing σ_A-weighted $mF_o - DF_c$ maps and the contour level is 3σ. Prior to map calculation, heavy chain residues 94–101, along with surrounding residues within 3.9 Å, were omitted from the model and simulated annealing was performed. Note that residues 98–100A (RPYY) are disordered, and they appear in the deposited PDB entries with occupancy of zero. A theoretical model of the backbone of residues 98–100A is drawn to help guide the eye.

consecutive T nucleotides, it provides a good model for the local interactions between 11F8 and the loop of the stem–loop ligand. Modeling of this interaction is potentially important because the pathogenicity of 11F8 has been demonstrated by mouse studies showing that 11F8 localizes to kidney tissue by binding to DNA adherent to the glomerular basement membrane.[7]

Plasticity of HCDR3

A major result of this work is that HCDR3 is intrinsically unstructured in the absence of bound ligand, and that conformational ordering occurs upon ligand binding. Crystallographic disorder in HCDR3 of the magnitude reported here is unusual, but not unprecedented. For example, Huang and co-workers recently reported three structures of anti-HIV CD4i Fabs containing disordered HCDR3 loops.[43] Complexes of these Fabs with bound ligands were not reported. Also, Buchbinder and co-workers reported the structure of a catalytic Ab Fab fragment with disorder in the apical residues of HCDR3 (residues H98–H100B).[44] Note that this is the same region of HCDR3 that is disordered in DNA-1.

The ligand-free structures help explain our recent structure of DNA-1 complexed with the buffer molecule Hepes (4-(2-hydroxyethyl)piperazine-1-ethanesulfonic acid).[45] The DNA-1/Hepes structures showed a 13 Å structural difference in the apex of HCDR3 compared to either the DNA-1/dT_5 or DNA-1/dT_3 structures. This is precisely the region of HCDR3 that is disordered in the ligand-free structures. Thus, we now see that the ability of DNA-1 to bind diverse ligands (oligo(dT) and Hepes) is due to the fact that HCDR3 is highly flexible in the absence of bound ligand. This inherent flexibility allows the Fab to radically modify the size and shape of the binding site to match the size and shape requirements of the ligand.

The large structural differences between the DNA-1/oligo(dT) and DNA-1/Hepes structures are similar in magnitude to those observed in two Fab structures of the germline precursor to Ab 7G12 bound to two different ligands, jeffamine and *N*-methylmesoporphyrin IX.[46] It was concluded that structural plasticity, particularly in HCDR3, underlies polyspecificity of the germline Ab, and that somatic mutation helps lock in a more rigid and optimal binding site.[46,47] We likewise conclude that conformational flexibility accounts for the polyspecificity of DNA-1.

Thermodynamics and mutagenesis

Our discovery that HCDR3 is intrinsically unstructured in the absence of bound ligand provides new insights into the molecular basis of previously reported thermodynamic data. The thermodynamics of oligo(dT) binding to DNA-1 have been investigated by fluorescence quenching[34] and isothermal titration calorimetry.[45] DNA-1 binds to dT_5 (298 K) with an apparent enthalpy change of $\Delta H = -17$ kcal/mol, while the entropy of association is unfavorable, $-T\Delta S = 10$ kcal/mol.[45] The ligand-free structures presented here suggest that the unfavorable entropy change is due, in part, to the conformational ordering of HCDR3 and the L92 side-chain during ligand binding.

The idea that ligand binding quenches motion of CDR loops has been discussed previously. For example, Kroon and co-workers used NMR to study changes in dynamics caused by ligand binding to a catalytic Ab Fv fragment.[48] They found evidence for significant motion of HCDR3 in the free Fv, and damping of LCDR3 backbone motion upon binding. Also, quenching of the mobility of a Lys side-chain has been described in Ab–protein recognition.[49]

Doig and Sternberg reviewed the contribution of side-chain conformational entropy in the context of protein folding, and concluded that the mean conformational entropy penalty is approximately 0.5 kcal/mol per rotatable bond.[50] Presumably, similar entropic penalties are involved in ligand binding to DNA-1. Tyr L92, Tyr H100, and Tyr H100A are disordered in the absence of ligand, but are ordered in the Fab/dT_3 complex, where they interact strongly with the ligand. Conformational ordering of these three side-chains alone contributes an estimated 3 kcal/mol to the total 10 kcal/mol $-T\Delta S$ of binding. This estimate represents a lower bound for the conformational entropy of binding due to the Fab because it does not consider the entropic penalty associated with stabilizing the backbone of HCDR3. Thus, the conformational ordering that we observe plays a very significant role in ligand recognition.

Our results also shed light on previous mutagenesis studies of Fab DNA-1. Mutation of Pro H99 to Gly, Tyr, or Arg decreases affinity by increasing the entropy of binding penalty by $\Delta(-T\Delta S) = 1$–6 kcal/mol.[34] Based on our structures, we argue that removal of Pro allows HCDR3 to explore a greater volume of conformational space, which would lead to an increased conformational entropy penalty due to ordering of HCDR3 upon binding. This situation is analogous to the well-known phenomenon in the protein folding field that mutation to Pro increases protein stability by decreasing the conformational entropy of unfolding.[51–54]

Mechanism of ssDNA recognition

Two observations suggest that DNA-1 has a complex binding mechanism, one in which protein motion plays an important role. First, HCDR3 is disordered in our ligand-free crystal structures, which suggests that HCDR3 is very flexible and adopts more than one conformation in solution. Second, we previously observed two very different conformations of HCDR3 in complex with oligo(dT) and Hepes.[45] Thus, it is unlikely that DNA-1 obeys a simple lock and key mechanism of binding.

Induced fit is the most commonly discussed binding mechanism that involves motion of the Ab. Induced fit binding for antibodies was first suggested by structures of a Bence-Jones dimer,[55,56] and later described in detail for the anti-peptide Fab 17/9 by Wilson's group.[57–59] In the simplest induced fit scenario, the ligand-free Ab adopts a single conformation, and binding causes structural

changes in the Ab and/or ligand that lead to an improved binding geometry.[60]

Edmundson's group has provided structural evidence for induced fit binding in antibody-ssDNA recognition.[32] Their work focused on Fab BV04-01, which was derived from an Ab obtained from an autoimmune NZB/NZW mouse. Fab BV04-01 displays a binding preference for T-rich ssDNA ligands, and binds to dT_6 with K_d = 130 nM.[61,62] Crystal structures of BV04-01 complexed with $d(pT)_3$ and in the ligand-free state showed that ligand binding causes local conformational changes in LCDR1 and HCDR3, along with small domain shifts of the V_L and V_H domains.[32] The local changes include 2–3 Å movements of LCDR1 and HCDR3 to accommodate the ligand, and side-chain reorientation of Trp H100A. Importantly, all six CDRs of BV04-01 are well ordered in the absence of bound ligand, and there is no evidence for multiple CDR conformations of the ligand-free Fab. Likewise, in the case of Fab 17/9, which may be considered the prototypical example of induced fit binding for antibodies, there is no evidence of multiple CDR conformations in either the ligand-free or bound forms.[58]

Fab DNA-1 is somewhat different from BV04-01 and 17/9, in that HCDR3 apparently adopts multiple conformations in the ligand-free state, as suggested by the disorder we observe for HCDR3 in the two ligand-free structures presented here. Thus, DNA-1 may represent a rather extreme case of induced fit in which ligand binding is accompanied by folding of HCDR3. Dyson and Wright have described several examples of biomolecular association in which ligand binding is coupled to folding of the receptor.[63,64] In fact, this mechanism of ligand recognition has been observed previously for nucleic acid-binding proteins. For example, ribosomal protein L11 features a loop that is unstructured in the free protein, but highly ordered when bound to RNA.[65] It is argued that local folding upon binding provides a unique regulatory mechanism for controlling transcription and translation. In particular, intrinsic flexibility allows regulatory proteins to bind different targets with high affinity.[64] Whereas this may be an advantage for nucleic acid-binding regulatory proteins, it could be a disadvantage for antibodies. In the context of autoimmune disease, plasticity of the ligand-free state could provide a mechanism by which anti-DNA antibodies bind diverse host ligands, and therefore contribute to pathogenicity.

Our structural data are also consistent with the theory of pre-existing isomeric equilibrium, which postulates an equilibrium between different structural isomers of the ligand-free Ab, with each isomer potentially providing a different binding site.[60,66,67] The ensemble of conformational isomers thus represents a source of antibody diversity at the protein level, in addition to gene-level diversity. Foote and Milstein provided convincing kinetic data in support of pre-existing equilibrium several years ago,[60] but structural evidence has only recently been obtained.[66]

The crystallographic disorder we observe for HCDR3 and LCDR3 suggests that the ligand-free Fab exhibits multiple conformations, which is consistent with pre-existing equilibrium. Moreover, we also observed very different conformations of HCDR3 when comparing structures of the Fab complexed with oligo(dT) and Hepes.[45] It is tempting to speculate that these two conformations represent two isomers that existed before ligand binding.

Whether ligand recognition by DNA-1 is a case of extreme induced fit or pre-existing equilibrium cannot be answered by structural data alone. Detailed analysis of binding kinetics is required, as has been done for other Abs by Foote and Milstein[60] and James *et al*.[66] Nonetheless, it is clear that plasticity of HCDR3 plays a central role in recognition of ssDNA and non-DNA ligands by Fab DNA-1. Our results also imply that CDR plasticity should be considered as an important factor underlying the cross-reactivity of other anti-DNA antibodies.

Finally, the observed plasticity of HCDR3 suggests that it is highly unlikely that theoretical modeling can provide reliable three-dimensional models of anti-ssDNA combining sites. Current modeling programs would certainly not have predicted the high degree of flexibility that we observed in HCDR3. Thus, there remains an important need for more crystal structures of anti-ssDNA antibodies.

Materials and Methods

Crystallization

Fab DNA-1 was expressed in *Escherichia coli* and purified as described.[68] Prior to crystallization, DNA-1 was dialyzed into 10 mM Tris–HCl (pH 7.0), 50 mM NaCl, and concentrated to 17 mg/ml using a stirred ultrafiltration cell. dT_3 was purchased from Research Genetics, Inc., and dissolved in 48 mM NaOH to achieve an 8–10 mM stock solution.

The Fab/dT_3 complex was formed by incubating the protein in a 7–8 molar excess of dT_3. Crystals of DNA-1/dT_3 were grown in sitting drops at room temperature using a reservoir solution of 1.8–2.1 M ammonium sulfate, 0.05–0.1 M sodium phosphate, 0.05–0.1 M sodium citrate buffer (pH 4.5–5.4). This recipe was identified using crystal screening, and it is similar to the recipe used to crystallize DNA-1/dT_5 (2 M ammonium sulfate, 0.1 M sodium acetate, pH 5.0). The crystals were cryoprotected by soaking them in 2 M ammonium sulfate, 0.05 M sodium phosphate, 0.05 M sodium citrate buffer (pH 5.0), and 30% (v/v) glycerol. The crystals were frozen by plunging them directly into liquid nitrogen. The crystals have the same unit cell and space group as DNA-1/dT_5 crystals.[68] The space group is $P6_522$ with cell dimensions a = 170.7 Å, c = 144.7 Å. The asymmetric unit contains two Fabs, with a solvent content of 60% (v/v).

Two crystal forms of the ligand-free Fab were obtained using conditions initially identified by crystal screening.

Table 2. R_{merge} statistics for the twinned data set in various space groups

Resolution range (Å)	*P*3	*P*312	*P*321	*P*6	*P*622
50.0–5.38	0.049	0.041	0.041	0.052	0.044
5.38–4.27	0.065	0.056	0.054	0.070	0.058
4.27–3.73	0.079	0.070	0.069	0.086	0.075
3.73–3.39	0.104	0.088	0.087	0.110	0.094
3.39–3.15	0.125	0.116	0.116	0.134	0.124
3.15–2.96	0.174	0.160	0.160	0.183	0.179
2.96–2.82	0.228	0.217	0.218	0.240	0.232
2.82–2.69	0.331	0.315	0.314	0.350	0.346
2.69–2.59	0.424	0.386	0.385	0.447	0.413
2.59–2.50	0.559	0.513	0.511	0.594	0.543
Overall	0.094	0.091	0.090	0.103	0.095

The $P6_5$ crystal form was grown in sitting drops at room temperature using a reservoir solution of 20% isopropanol, 14% (w/v) PEG 4000, and 0.1 M sodium citrate (pH 5.5). The crystals were cryoprotected in 20% isopropanol, 20% PEG 4000, 0.1 M sodium citrate (pH 5.6), 10% PEG 200, and then plunged into liquid nitrogen. The crystals exhibit space group $P6_5$ with cell dimensions $a=201.8$ Å, $c=44.8$ Å. The asymmetric unit contains two Fabs with a solvent content of 55%.

The *P*321 ligand-free crystals grew as thin hexagonal plates, and appeared in many crystal screen solutions containing ammonium sulfate. Small, thin hexagonal plates (0.1 mm×0.1 mm×0.05 mm) were grown using a reservoir solution of 1.5 M ammonium sulfate, 0.1 M sodium acetate (pH 4.9). Over a period of two months, the reservoir solution was replaced with 2.0 M ammonium sulfate in 0.25 M increments. This technique produced crystals of 0.1 mm in all dimensions. These crystals were seeded into drops containing fresh protein and 1.0–1.4 M ammonium sulfate, which produced diffraction quality crystals. These crystals were cryoprotected in the harvest solution (2.0 M ammonium sulfate, 0.1 M sodium acetate, pH 5.0) supplemented with 30% glycerol. The cryoprotected crystals were plunged into liquid nitrogen. The space group is *P*321 with unit cell dimensions $a=179.2$ Å, $c=91.9$ Å. There are two Fabs per asymmetric unit and the solvent content is 70% (v/v).

Data collection and refinement

X-ray diffraction data sets for use in structure refinement calculations were recorded at beamlines X8C and X12C of the National Synchrotron Light Source. Data extending to 2.3 Å resolution were obtained from the DNA-1/dT_3 and $P6_5$ crystals. The *P*321 crystals diffracted to 2.5 Å resolution. In addition, a highly redundant, lower resolution data set was collected from a DNA-1/dT_3 crystal using an in-house CuK_α system. These data were used to identify the locations of phosphate atoms of the DNA ligand using anomalous difference Fourier analysis as described.[69] The anomalous difference Fourier map was calculated using phases from the final structure and anomalous differences to 4.0 Å resolution. All data sets were processed with HKL or HKL2000.[70] See Table 1 for data collection statistics.

Molecular replacement calculations were performed with AMoRe.[71] Structure refinements were performed with CNS[72] and REFMAC5 (including TLS).[73–75] Model building was done with O.[76] Structure analysis was performed with PyMol,† CNS, and O.

Structure refinement of DNA-1/dT_3 was initiated from the coordinates of the previously solved DNA-1/dT_5 structure, with DNA and solvent atoms removed. The test set of reflections used for R_{free} calculations corresponded to that used for refinement of DNA-1/dT_5. The occupancy of the dT_3 ligand was estimated from alternating cycles of *B*-factor and occupancy refinement in CNS as suggested by Jensen.[77] The resulting value was 0.9, which is similar to the occupancy of dT_5 in the DNA-1/dT_5 structure.

The ligand-free structures were determined by molecular replacement using search models extracted from the coordinates of the 1.75 Å DNA-1/Hepes complex structure (PDB entry 1P7K).[45] Structure determination of the $P6_5$ crystal form was straightforward, but twinning complicated analysis of the *P*321 data, as described next.

Structure determination using twinned crystals

Perfect hemihedral twinning complicated structure determination of the *P*321 crystal form. Although several protein structures have been solved using twinned crystals, the use of twinned data is still somewhat uncommon.[38–42] Therefore, some of the details of structure determination are presented here.

The data exhibited apparent 6/mmm Laue symmetry, as evidenced by the nearly equivalent merging statistics obtained in space groups *P*622, *P*321, *P*312, *P*6, and *P*3 (Table 2). Attempts to solve the structure using molecular replacement (MR) in space groups having 6/mmm Laue symmetry failed. Whereas an MR solution with reasonable correlation coefficient could be obtained in space group *P*622, the packing revealed badly overlapping molecules. Therefore, the possibility of twinning was considered.

Several tests were performed to detect the presence of twinning in the data. The data set, merged in space group *P*622, was uploaded to the Yeates and Fam Twinning Server at UCLA to determine if the intensity statistics followed the expected Wilson statistics.[41] The perfect merohedral twinning test returned an average value of $\langle I^2(h)\rangle/\langle I(h)\rangle^2=1.6(\pm0.1)$, for all data to 2.5 Å resolution. For reference, a value of 1.5 indicates perfect twinning, and a value of 2.0 indicates no twinning.[41] Note that values of this twinning indicator for the DNA-1/dT_3 and $P6_5$ data sets were 2.1($\pm$0.2) and 1.9($\pm$0.1), respectively, which indicated lack of twinning in those crystals. The twinning fraction estimated from the UCLA server for the *P*321 data set using the partial merohedral twinning test was 0.48. Likewise, the partial twinning test of CNS returned a twinning fraction of 0.47. Also, the cumulative intensity distribution[78] was calculated using the TRUNCATE module of the CCP4 suite. The distribution for

† http://pymol.sourceforge.net

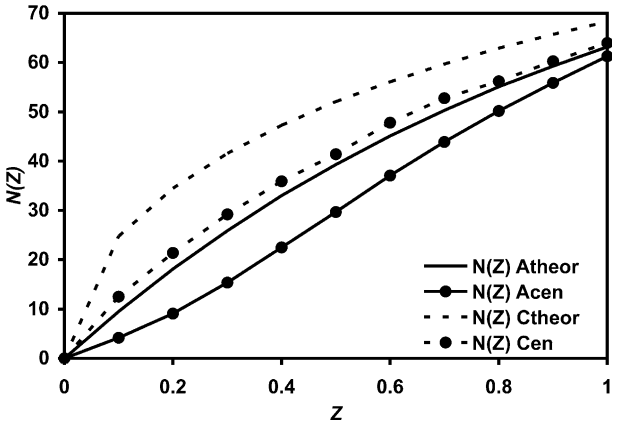

Figure 7. Cumulative intensity distribution[78] calculated for the twinned data set merged in space group *P*321. *N*(*Z*) is the number of reflections with relative intensity less than *Z*. The data for this plot were generated with the TRUNCATE module of CCP4.[73] The continuous and broken curves were obtained from acentric, and centric data, respectively. Curves with filled circles represent our experimental data. Curves without filled circles represent the expected theoretical distribution. Note the sigmoidal shape of the curve for experimental acentric reflections (continuous curve, filled circles), which is indicative of twinning.

acentric reflections clearly exhibited the sigmoidal shape indicative of twinning (Figure 7).

The aforementioned statistical indicators strongly suggested hemihedral twinning with a twinning fraction (α) very close to 0.5, and therefore perfect hemihedral twinning ($\alpha = 0.5$) was assumed. In the case of perfect hemihedral twinning, a model is required for the detwinning procedure[41] and thus MR calculations were performed using the twinned diffraction data. Since the correct space group was not known, all possible space groups having 3-fold or 6-fold symmetry had to be considered during MR calculations. The solvent content was estimated using the Matthews method[79] to see whether any of the space groups could be eliminated based on crystal-packing considerations, as suggested by Dauter.[39] This approach was used by Luecke *et al.* in the case of bacteriorhodopsin to eliminate space groups with 6/mmm Laue symmetry.[80] In our case, however, the solvent content was plausible (45–72%) for all space groups tested (Table 3).

Molecular replacement calculations were thus performed in the various trigonal and hexagonal space groups, and the correlation coefficient and *R*-factor from AMoRe were monitored. All of the space groups yielded plausible solutions, as indicated by correlation coefficients (CC) greater than 0.3 and *R*-factors below 0.5. However, the statistics for three space groups (*P*6, *P*312, and *P*321) were markedly better, with CC > 0.5 and *R*-factor < 0.41 (Table 3). The solution for space group *P*321 had the highest CC (0.62) and lowest *R*-factor (0.37).

Packing diagrams for several of the top solutions were generated and viewed graphically. The top solutions for space groups *P*622, *P*6, and *P*312 had badly overlapped molecules, which indicated that these solutions were wrong despite having good MR statistics. Only the *P*321 solution exhibited acceptable packing. Electron density maps for the best solutions in *P*622, *P*6, *P*312, and *P*321 were calculated after detwinning the data using CNS. Since the twin fraction was very close to 0.5, perfect hemihedral twinning was assumed during the detwinning procedure (CNS script detwin_perfect.inp), as advised previously.[41] Visual inspection of the maps readily showed that the density was discontinuous for the main chain and completely lacking for side-chains in space groups *P*622, *P*6, and *P*312. Only the *P*321 solution yielded a map with continuous density for the main chain and distinct side-chain density (Figure 1). *P*321 was thus deemed the correct space group, with twinning operator $(-h, -k, l)$.

The structure was improved through iterative rounds of model building, detwinning the original diffraction data using CNS, and refinement in CNS or REFAC5 using the detwinned data. The CNS script, make_cv_twin.inp, was used to select a test set of reflections for structure refinement. The detwinning step in the final round lowered R_{cryst} and R_{free} by 0.111 and 0.099, respectively, which confirmed the presence of twinning in the data, and supported the use of detwinning procedures.

PDB accession code

The atomic coordinates and structure factors have been deposited in the RCSB Protein Data Bank[81] as entries 1XF2, 1XF3, and 1XF4.

Acknowledgements

We thank the personnel of NSLS beamlines X8C and X12C for their assistance with data collection.

Table 3. Summary of the top molecular replacement solutions for the twinned structure

Space group	Molecules per asymmetric unit	Solvent content (%, v/v)	Correlation coefficient	*R*-factor
*P*622	1	72	0.470	0.435
*P*622	2	45	0.481	0.431
*P*6	1	86	0.373	0.463
*P*6	2	72	0.474	0.430
*P*6	3	58	0.522	0.407
*P*6	4	45	0.585	0.383
*P*312	1	86	0.480	0.428
*P*312	2	72	0.544	0.405
*P*312	3	58	0.599	0.380
*P*321	1	86	0.453	0.435
*P*321	2	72	0.625	0.368

This research was supported, in part, by a grant from the University of Missouri Research Board to J.J.T. Part of this research was carried out at the National Synchrotron Light Source, Brookhaven National Laboratory, which is supported by the U.S. Department of Energy, Division of Materials Sciences and Division of Chemical Sciences, under contract no. DE-AC02-98CH10886.

References

1. Stollar, B. D. (1981). Anti-DNA antibodies. *Clin. Immunol. Allergy*, **1**, 243–260.
2. Amoura, Z., Koutouzov, S. & Piette, J. C. (2000). The role of nucleosomes in lupus. *Curr. Opin. Rheumatol.* **12**, 369–373.
3. Jang, Y. J. & Stollar, B. D. (2003). Anti-DNA antibodies: aspects of structure and pathogenicity. *Cell. Mol. Life Sci.* **60**, 309–320.
4. Pisetsky, D. S., Grudier, J. P. & Gilkeson, G. S. (1990). A role for immunogenic DNA in the pathogenesis of systemic lupus erythematosus. *Arthritis Rheum.* **33**, 153–159.
5. Winfield, J. B., Faiferman, I. & Koffler, D. (1991). Avidity of anti-DNA antibodies in serum and IgG glomerular eluates from patients with systemic lupus erythematosus. Associations of high avidity anti-native DNA antibody with glomerulonephritis. *J. Clin. Invest.* **59**, 90–95.
6. Murakami, H., Lam, Z., Furie, B. C., Reinhold, V. N., Asano, T. & Furie, B. (1991). Sulfated glycolipids are the platelet autoantigens for human platelet-binding monoclonal anti-DNA autoantibodies. *J. Biol. Chem.* **266**, 15414–15419.
7. Swanson, P. C., Yung, R. L., Blatt, N. B., Eagan, M. A., Norris, J. M., Richardson, B. C. *et al*. (1996). Ligand recognition by murine anti-DNA autoantibodies. II. Genetic analysis and pathogenicity. *J. Clin. Invest.* **97**, 1748–1760.
8. Blatt, N. B. & Glick, G. D. (1999). Anti-DNA autoantibodies and systemic lupus erythematosus. *Pharmacol. Ther.* **83**, 125–139.
9. Waer, M. (1990). The role of anti-DNA antibodies in lupus nephritis. *Clin. Rheumatol. Suppl. 1*, **9**, 111–114.
10. Isenberg, D. A., Ehrenstein, M. R., Longhurst, C. & Kalsi, J. K. (1994). The origin, sequence, structure, and consequences of developing anti-DNA antibodies. A human perspective. *Arthritis Rheum.* **37**, 169–180.
11. Eilat, D. & Anderson, W. F. (1994). Structure-function correlates of autoantibodies to nucleic acids. Lessons from immunochemical, genetic and structural studies. *Mol. Immunol.* **31**, 1377–1390.
12. Rahman, A., Kumar, S. & Potter, K. N. (2002). Anti-DNA antibodies–structure and function. *Lupus*, **11**, 776–779.
13. Jones, D. S., Barstad, P. A., Feild, M. J., Hachmann, J. P., Hayag, M. S., Hill, K. W. *et al*. (1995). Immunospecific reduction of antioligonucleotide antibody-forming cells with a tetrakis-oligonucleotide conjugate (LJP 394), a therapeutic candidate for the treatment of lupus nephritis. *J. Med. Chem.* **38**, 2138–2144.
14. Linnik, M., Staines, N. A., Berden, J. & Isenberg, D. A. (2002). Workshop report on some new ideas about the treatment of systemic lupus erythematosus. *Lupus*, **11**, 793–796.
15. Ben-Chetrit, E., Eilat, D. & Ben-Sasson, S. A. (1988). Specific inhibition of the DNA-anti-DNA immune reaction by low molecular weight anionic compounds. *Immunology*, **65**, 479–485.
16. Kowal, C., Weinstein, A. & Diamond, B. (1999). Molecular mimicry between bacterial and self antigen in a patient with systemic lupus erythematosus. *Eur. J. Immunol.* **29**, 1901–1911.
17. Sharma, A., Isenberg, D. A. & Diamond, B. (2001). Crossreactivity of human anti-dsDNA antibodies to phosphorylcholine: clues to their origin. *J. Autoimmun.* **16**, 479–484.
18. Mostoslavsky, G., Fischel, R., Yachimovich, N., Yarkoni, Y., Rosenmann, E., Monestier, M. *et al*. (2001). Lupus anti-DNA autoantibodies cross-react with a glomerular structural protein: a case for tissue injury by molecular mimicry. *Eur. J. Immunol.* **31**, 1221–1227.
19. Gaynor, B., Putterman, C., Valadon, P., Spatz, L., Scharff, M. D. & Diamond, B. (1997). Peptide inhibition of glomerular deposition of an anti-DNA antibody. *Proc. Natl Acad. Sci. USA*, **94**, 1955–1960.
20. DeGiorgio, L. A., Konstantinov, K. N., Lee, S. C., Hardin, J. A., Volpe, B. T. & Diamond, B. (2001). A subset of lupus anti-DNA antibodies cross-reacts with the NR2 glutamate receptor in systemic lupus erythematosus. *Nature Med.* **7**, 1189–1193.
21. Sibille, P., Ternynck, T., Nato, F., Buttin, G., Strosberg, D. & Avrameas, A. (1997). Mimotopes of polyreactive anti-DNA antibodies identified using phage-display peptide libraries. *Eur. J. Immunol.* **27**, 1221–1228.
22. Calcutt, M. J., Kremer, M. T., Giblin, M. F., Quinn, T. P. & Deutscher, S. L. (1993). Isolation and characterization of nucleic acid-binding antibody fragments from autoimmune mice-derived bacteriophage display libraries. *Gene*, **137**, 77–83.
23. Thiebe, R., Schable, K. F., Bensch, A., Brensing-Kuppers, J., Heim, V., Kirschbaum, T. *et al*. (1999). The variable genes and gene families of the mouse immunoglobulin kappa locus. *Eur. J. Immunol.* **29**, 2072–2081.
24. Schable, K. F., Thiebe, R., Bensch, A., Brensing-Kuppers, J., Heim, V., Kirschbaum, T. *et al*. (1999). Characteristics of the immunoglobulin Vkappa genes, pseudogenes, relics and orphons in the mouse genome. *Eur. J. Immunol.* **29**, 2082–2086.
25. Haines, B. B., Angeles, C. V., Parmelee, A. P., McLean, P. A. & Brodeur, P. H. (2001). Germline diversity of the expressed BALB/c VhJ558 gene family. *Mol. Immunol.* **38**, 9–18.
26. Lefranc, M. P. (2003). IMGT, the international ImMunoGeneTics database. *Nucl. Acids Res.* **31**, 307–310.
27. Swanson, P. C., Ackroyd, C. & Glick, G. D. (1996). Ligand recognition by anti-DNA autoantibodies. Affinity, specificity, and mode of binding. *Biochemistry*, **35**, 1624–1633.
28. Stevens, S. Y. & Glick, G. D. (1999). Evidence for sequence-specific recognition of DNA by anti-single-stranded DNA autoantibodies. *Biochemistry*, **38**, 560–568.
29. Ackroyd, P. C., Cleary, J. & Glick, G. D. (2001). Thermodynamic basis for sequence-specific recognition of ssDNA by an autoantibody. *Biochemistry*, **40**, 2911–2922.
30. Cleary, J. & Glick, G. D. (2003). Mutational analysis of a sequence-specific ssDNA binding lupus autoantibody. *Biochemistry*, **42**, 30–41.
31. Swanson, P. C., Cooper, B. C. & Glick, G. D. (1994).

High resolution epitope mapping of an anti-DNA autoantibody using model DNA ligands. *J. Immunol.* **152**, 2601–2612.
32. Herron, J. N., He, X. M., Ballard, D. W., Blier, P. R., Pace, P. E., Bothwell, A. L. M. *et al*. (1991). An autoantibody to single-stranded DNA: comparison of the three-dimensional structures of the unliganded Fab and a deoxynucleotide-Fab complex. *Proteins: Struct. Funct. Genet.* **11**, 159–175.
33. Komissarov, A. A., Marchbank, M. T., Calcutt, M. J., Quinn, T. P. & Deutscher, S. L. (1997). Site-specific mutagenesis of a recombinant anti-single-stranded DNA Fab. Role of heavy chain complementarity-determining region 3 residues in antigen interaction. *J. Biol. Chem.* **272**, 26864–26870.
34. Komissarov, A. A. & Deutscher, S. L. (1999). Thermodynamics of Fab/DNA interactions: contributions of heavy chain complementarity determining region 3. *Biochemistry*, **38**, 14631–14637.
35. Tanner, J. J., Komissarov, A. A. & Deutscher, S. L. (2001). Crystal structure of an antigen-binding fragment bound to single-stranded DNA. *J. Mol. Biol.* **314**, 807–822.
36. Kabat, E. A., Wu, T. T., Perry, H. M., Gottesmann, K. S. & Foeller, C. (1991). *Sequences of Proteins of Immunological Interest*, 5th edit., National Institutes of Health, Bethesda, MD.
37. Martin, A. C. (1996). Accessing the Kabat antibody sequence database by computer. *Proteins: Struct. Funct. Genet*, **25**, 130–133.
38. Chandra, N., Acharya, K. R. & Moody, P. C. (1999). Analysis and characterization of data from twinned crystals. *Acta Crystallog. sect. D*, **55**, 1750–1758.
39. Dauter, Z. (2003). Twinned crystals and anomalous phasing. *Acta Crystallog. sect. D*, **59**, 2004–2016.
40. Parsons, S. (2003). Introduction to twinning. *Acta Crystallog. sect. D*, **59**, 1995–2003.
41. Yeates, T. O. (1997). Detecting and overcoming crystal twinning. *Methods Enzymol.* **276**, 344–358.
42. Yeates, T. O. & Fam, B. C. (1999). Protein crystals and their evil twins. *Struct. Fold. Des.* **7**, R25–R29.
43. Huang, C. C., Venturi, M., Majeed, S., Moore, M. J., Phogat, S., Zhang, M. Y. *et al*. (2004). Structural basis of tyrosine sulfation and VH-gene usage in antibodies that recognize the HIV type 1 coreceptor-binding site on gp120. *Proc. Natl Acad. Sci. USA*, **101**, 2706–2711.
44. Buchbinder, J. L., Stephenson, R. C., Scanlan, T. S. & Fletterick, R. J. (1998). A comparison of the crystallographic structures of two catalytic antibodies with esterase activity. *J. Mol. Biol.* **282**, 1033–1041.
45. Schuermann, J. P., Henzl, M. T., Deutscher, S. L. & Tanner, J. J. (2004). Structure of an anti-DNA fab complexed with a non-DNA ligand provides insights into cross-reactivity and molecular mimicry. *Proteins: Struct. Funct. Genet.* **57**, 269–278.
46. Yin, J., Beuscher, A. E. t., Andryski, S. E., Stevens, R. C. & Schultz, P. G. (2003). Structural plasticity and the evolution of antibody affinity and specificity. *J. Mol. Biol.* **330**, 651–656.
47. Wedemayer, G. J., Patten, P. A., Wang, L. H., Schultz, P. G. & Stevens, R. C. (1997). Structural insights into the evolution of an antibody combining site. *Science*, **276**, 1665–1669.
48. Kroon, G. J., Mo, H., Martinez-Yamout, M. A., Dyson, H. J. & Wright, P. E. (2003). Changes in structure and dynamics of the Fv fragment of a catalytic antibody upon binding of inhibitor. *Protein Sci.* **12**, 1386–1394.
49. Li, Y., Urrutia, M., Smith-Gill, S. J. & Mariuzza, R. A. (2003). Dissection of binding interactions in the complex between the anti-lysozyme antibody HyHEL-63 and its antigen. *Biochemistry*, **42**, 11–22.
50. Doig, A. J. & Sternberg, M. J. (1995). Side-chain conformational entropy in protein folding. *Protein Sci.* **4**, 2247–2251.
51. Matthews, B. W., Nicholson, H. & Becktel, W. J. (1987). Enhanced protein thermostability from site-directed mutations that decrease the entropy of unfolding. *Proc. Natl Acad. Sci. USA*, **84**, 6663–6667.
52. Herning, T., Yutani, K., Inaka, K., Kuroki, R., Matsushima, M. & Kikuchi, M. (1992). Role of proline residues in human lysozyme stability: a scanning calorimetric study combined with X-ray structure analysis of proline mutants. *Biochemistry*, **31**, 7077–7085.
53. Hardy, F., Vriend, G., Veltman, O. R., van der Vinne, B., Venema, G. & Eijsink, V. G. (1993). Stabilization of Bacillus stearothermophilus neutral protease by introduction of prolines. *FEBS Letters*, **317**, 89–92.
54. Li, Y., Reilly, P. J. & Ford, C. (1997). Effect of introducing proline residues on the stability of *Aspergillus awamori*. *Protein Eng.* **10**, 1199–1204.
55. Edmundson, A. B., Ely, K. R., Girling, R. L., Abola, E. E., Schiffer, M., Westholm, F. A. *et al*. (1974). Binding of 2,4-dinitrophenyl compounds and other small molecules to a crystalline lambda-type Bence-Jones dimer. *Biochemistry*, **13**, 3816–3827.
56. Davies, D. R. & Padlan, E. A. (1992). Twisting into shape. *Curr. Biol.* **2**, 254–256.
57. Schulze-Gahmen, U., Rini, J. M. & Wilson, I. A. (1993). Detailed analysis of the free and bound conformations of an antibody. X-ray structures of Fab 17/9 and three different Fab-peptide complexes. *J. Mol. Biol.* **234**, 1098–1118.
58. Rini, J. M., Schulze-Gahmen, U. & Wilson, I. A. (1992). Structural evidence for induced fit as a mechanism for antibody-antigen recognition. *Science*, **255**, 959–965.
59. Wilson, I. A. & Stanfield, R. L. (1994). Antibody–antigen interactions: new structures and new conformational changes. *Curr. Opin. Struct. Biol.* **4**, 857–867.
60. Foote, J. & Milstein, C. (1994). Conformational isomerism and the diversity of antibodies. *Proc. Natl Acad. Sci. USA*, **91**, 10370–10374.
61. Rumbley, C. A., Denzin, L. K., Yantz, L., Tetin, S. Y. & Voss, E. W., Jr (1993). Construction, characterization, and selected site-specific mutagenesis of an anti-single-stranded DNA single chain autoantibody. *J. Biol. Chem.* **268**, 13667–13674.
62. Tetin, S. Y., Rumbley, C. A., Hazlett, T. L. & Voss, E. W., Jr (1993). Elucidation of anti-ssDNA autoantibody BV 04-01 binding interactions with homooligonucleotides. *Biochemistry*, **32**, 9011–9017.
63. Dyson, H. J. & Wright, P. E. (2002). Coupling of folding and binding for unstructured proteins. *Curr. Opin. Struct. Biol.* **12**, 54–60.
64. Wright, P. E. & Dyson, H. J. (1999). Intrinsically unstructured proteins: re-assessing the protein structure-function paradigm. *J. Mol. Biol.* **293**, 321–331.
65. Markus, M. A., Hinck, A. P., Huang, S., Draper, D. E. & Torchia, D. A. (1997). High resolution solution structure of ribosomal protein L11-C76, a helical protein with a flexible loop that becomes structured upon binding to RNA. *Nature Struct. Biol.* **4**, 70–77.
66. James, L. C., Roversi, P. & Tawfik, D. S. (2003). Antibody multispecificity mediated by conformational diversity. *Science*, **299**, 1362–1367.
67. Foote, J. (2003). Immunology. Isomeric antibodies. *Science*, **299**, 1327–1328.

68. Prewitt, S. P., Komissarov, A. A., Deutscher, S. L. & Tanner, J. J. (2000). Crystallization and molecular replacement studies of a recombinant antigen-binding fragment complexed with single-stranded DNA. *Acta Crystallog. sect. D*, **56**, 1007–1011.
69. Schuermann, J. P. & Tanner, J. J. (2003). MRSAD: using anomalous dispersion from S atoms collected at Cu Kalpha wavelength in molecular-replacement structure determination. *Acta Crystallog. sect. D*, **59**, 1731–1736.
70. Otwinowski, Z. & Minor, W. (1997). Processing of X-ray diffraction data collected in oscillation mode. *Methods Enzymol.* **276**, 307–326.
71. Navaza, J. (2001). Implementation of molecular replacement in AMoRe. *Acta Crystallog. sect. D*, **57**, 1367–1372.
72. Brünger, A. T., Adams, P. D., Clore, G. M., DeLano, W. L., Gros, P., Grosse-Kunstleve, R. W. *et al*. (1998). Crystallography and NMR system: a new software suite for macromolecular structure determination. *Acta Crystallog. sect. D*, **54**, 905–921.
73. Collaborative Computing Project Number 4. The CCP4 suite: programs for protein crystallography. *Acta Crystallog. sect. D*, **50**, 760–763.
74. Winn, M. D., Murshudov, G. N. & Papiz, M. Z. (2003). Macromolecular TLS refinement in REFMAC at moderate resolutions. *Methods Enzymol.* **374**, 300–321.
75. Winn, M. D., Isupov, M. N. & Murshudov, G. N. (2001). Use of TLS parameters to model anisotropic displacements in macromolecular refinement. *Acta Crystallog. sect. D*, **57**, 122–133.
76. Jones, T. A., Zou, J.-Y., Cowan, S. W. & Kjeldgaard, M. (1991). Improved methods for building protein models in electron density maps and the location of errors in these models. *Acta Crystallog. sect. A*, **47**, 110–119.
77. Jensen, L. H. (1990). Solvent model for protein crystals: on occupancy parameters for discrete solvent sites and the solvent continuum. *Acta Crystallog. sect. B*, **46**, 650–653.
78. Rees, D. C. (1980). The influence of twinning by merohedry on intensity statistics. *Acta Crystallog. sect. A*, **36**, 578–581.
79. Matthews, B. W. (1968). Solvent content of protein crystals. *J. Mol. Biol.* **33**, 491–497.
80. Luecke, H., Richter, H. T. & Lanyi, J. K. (1998). Proton transfer pathways in bacteriorhodopsin at 2.3 angstrom resolution. *Science*, **280**, 1934–1937.
81. Berman, H. M., Westbrook, J., Feng, Z., Gilliland, G., Bhat, T. N., Weissig, H. *et al*. (2000). The Protein Data Bank. *Nucl. Acids Res.* **28**, 235–242.
82. Engh, R. A. & Huber, R. (1991). Accurate bond and angle parameters for x-ray protein structure refinement. *Acta Crystallog. sect. A*, **47**, 392–400.
83. Laskowski, R. A., MacArthur, M. W., Moss, D. S. & Thornton, J. M. (1993). PROCHECK: a program to check the stereochemical quality of protein structures. *J. Appl. Crystallog.* **26**, 283–291.

Edited by I. Wilson

(Received 15 October 2004; received in revised form 28 December 2004; accepted 1 February 2005)